Measurement of excited-state charge exchange reactions

R. J. Knize,* S. R. Lundeen, and F. M. Pipkin
Lyman Laboratory of Physics, Harvard University, Cambridge, Massachusetts 02138
(Received 1 June 1983)

A microwave-resonance optical detection technique has been used to study the charge exchange reaction in which 49-keV protons incident on nitrogen and hydrogen molecules form hydrogen atoms in the $n=3$ state. Hydrogen atoms formed in the $n=3$ state in the charge exchange cell pass through a radio-frequency field, and the Balmer-α light emitted by the atoms is monitored. Measurements are made with the microwave electric field both perpendicular and parallel to the direction of the proton beam and for light polarized both parallel and perpendicular to the beam direction. Through a detailed analysis of the observed resonances, the partial cross sections for capture into each of the angular momentum states (L and M_L) are determined. The population of any state in the $n=3$ manifold can be calculated from these cross sections.

I. INTRODUCTION

The process where a proton captures an electron from a target atom or molecule to form a ground- or excited-state hydrogen atom is a basic collision reaction which is relevant to a wide area of pure and applied physics. Not only is this reaction a fundamental one which can be used to test our understanding of simple collisions, but there are many processes which are dependent on electron capture by protons. Charge exchange collisions are used to produce excited atoms for fast-beam precision measurements of the Lamb shift and fine structure of one-electron atoms[1,2] and to produce metastable beams for experiments searching for weak-interaction parity-violating effects in hydrogen.[3] Electron capture is important in thermonuclear fusion research for understanding atomic processes in plasmas, for production of intense neutral beams to heat the plasma, and for determining plasma parameters.[4] Charge exchange collisions are important in a wide variety of astrophysical phenomena ranging from the evolution of the early universe to the aurora borealis.[5]

Because of their importance, a great deal of effort has been devoted to measuring and calculating charge exchange cross sections.[6–11] The calculations are quite successful in the low-energy region where the velocity of the projectile is much less than the velocity of the orbiting electron and one can use a molecular-orbital approach and in the high-energy domain where one can use the Born approximation. It is still not clear, however, how to calculate the cross sections in the intermediate-energy range where the velocity of the projectile is comparable to the velocity of the orbiting electrons.[12–14] Much of this difficulty is centered on the correct treatment of the wave function for the electron which switches from the target atom to the projectile ion in the collision. This problem is usually referred to as the momentum-transfer problem. It may be necessary to carry out a full integration of the Schrödinger equation with no approximations to overcome this problem.[15,16] There are only a few calculations which provide the partial cross sections for capture into all the angular momentum substates belonging to a given principal quantum number and thus give a complete description of the charge capture collision.

A detailed test of the ability to calculate the cross section is provided by measurements of the partial cross sections for capture into each of the angular momentum states belonging to a given principal quantum number for protons incident on target atoms or molecules. Several measurements of the partial cross sections for capture into the $2s$ and $2p$ states of hydrogen which utilize the unique properties of the $n=2$ manifold[9,17,18] have been carried out. Some measurements of the partial cross sections for capture into the $n=3$ and 4 manifolds of hydrogen have been carried out using an analysis of the time dependence of the light emitted subsequent to an electron-capture collision to determine the partial cross sections.[19–21] These measurements are subject to large errors because of the difficulty of resolving a single observed decay curve unambiguously into the sum of three or more exponential curves.[22] The results are ambiguous due to the disagreements between the different observers. These experiments are limited in that they do not determine the partial cross sections for capture into each of the magnetic substates belonging to a particular angular momentum state.

This paper gives a complete report on an experiment which used a microwave-resonance optical detection (MROD) method to study excited-state electron-capture collisions for protons incident on hydrogen and nitrogen molecules. Using this method we have been able to determine the partial cross sections for capture into each of the L,M_L states for the $n=3$ manifold of hydrogen. This paper gives in succession an overview of the experiment, the theory for the experiment, a description of the apparatus, the procedure used to take data, the results of the measurements, and the conclusions. A preliminary report on the measurements for a nitrogen target has been published elsewhere.[23] The technique used can be traced to measurements carried out earlier on the $n=4$ manifold of hydrogen.[24–26]

 ©1984 The American Physical Society

II. OVERVIEW

Figure 1 shows a schematic diagram of the experiment. Fast protons enter the gas cell where some of them capture an electron through collisions with the gas molecules and form hydrogen atoms in an excited state. The excited-state atoms are detected downstream by a filter-polarizer-photomultiplier combination which measures the light from the states in a particular n manifold. An intervening microwave electric field is used to drive transitions between adjacent L levels within the n manifold being studied. The fractional change in the light emitted when a particular transition is driven gives a measure of the difference in population of the levels involved. Figure 2 shows the energy levels and observable electric dipole microwave transitions for the $n=3$ state of hydrogen. For each transition one observes the change in light intensity for the microwave electric field both parallel and perpendicular to the beam and for the emitted light polarized parallel and perpendicular to the beam. A precise understanding of the dependence of the observed signals on the populations of the atomic sublevels makes it possible to determine the partial cross sections for charge capture into each of the L,M_L states of a particular n manifold.

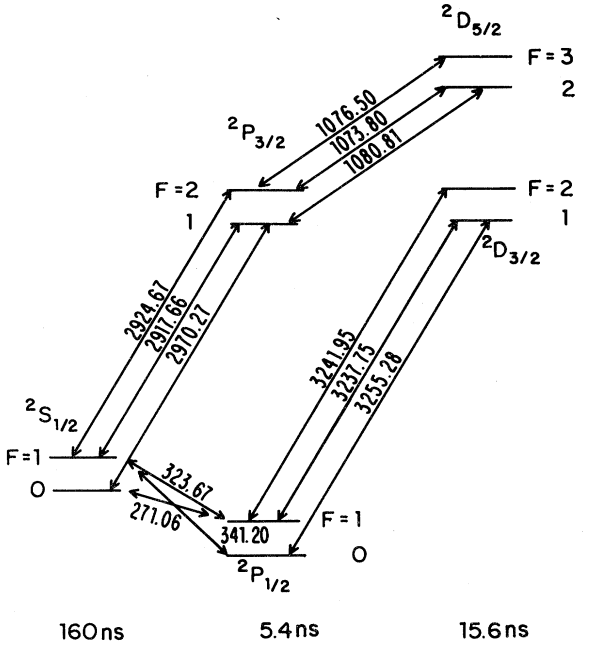

FIG. 2. Energy levels and allowed electric dipole transitions for the $n=3$ manifold of atomic hydrogen.

III. THEORY OF THE MEASUREMENT

The signal is defined as the fractional change in the light detected when the microwave field is switched on and off. In order to determine the electron-capture cross sections it is necessary to understand in detail how the signal depends on the state of the excited atom produced in a charge exchange collision. In this section we will calculate the signals for the situation in which a fast proton captures an electron in the target to form an excited atom, and after passing through a radio-frequency field the excited atom emits a photon which is detected. Our description of the signals is a generalization of earlier work of Silverman and Pipkin.[24–26] Even with an accurate knowledge of how the signals depend on the cross sections, it might not be possible to derive a unique value for the cross sections from the data. In the latter part of this section we examine the number of measurements required to determine uniquely the cross sections.

A. Electron-capture collisions

The electron-capture collisions between the fast incoming protons and the relatively stationary atoms or molecules take place in the target and produce fast excited hydrogen atoms which exit the target region. A complete description of the collision is given by the momenta and quantum states of both the initial proton and target atom and the final hydrogen atom and target ion. This experiment will be concerned with the situation where the incoming proton beam is monoenergetic and unpolarized, the initial target atom or molecule is relatively stationary and in the ground state, and the resultant cross sections are averaged over the states of the final target ion and integrated over the scattering angles. The result of the electron-capture collision is specified by the excited- and ground-state amplitudes of the hydrogen atom.

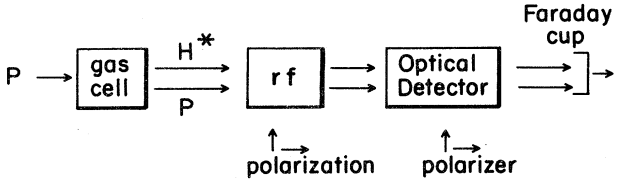

FIG. 1. Schematic diagram of the microwave resonance optical detection experiment used to study charge exchange collisions.

A complete description of the hydrogen atoms is given by the density operator $\hat{\rho}$. Neglecting coherences between different n manifolds there are $[2n^2(4n^2+1)-1]$ independent density-matrix elements for each manifold. For $n=3$, it requires 1295 real numbers to describe completely the most general density matrix. Since it is experimentally impractical to determine all these parameters general arguments must be used to simplify the density matrix. The Hamiltonian describing the collision will consist of kinetic, Coulombic, and spin-dependent terms. It is expected that to a good approximation the collision will not depend upon either the electron or proton spins. In the uncoupled angular momentum basis, n,L,S,I,M_L,M_S,M_I, this restricts the nonzero density-matrix elements to the following types:

$$\rho^{nLSIM_LM_SM_I}_{n'L'SIM'_LM'_SM'_I}=\rho^{nLM_L}_{n'L'M'_L}\delta_{M_SM'_S}\delta_{M_IM'_I}\ .$$

Since in the absence of any external fields the only preferred axis is the beam direction z and the initial target atom is in the ground state, the collision will possess rota-

tional symmetry around the z axis and reflection symmetry through any plane containing this axis. The first symmetry restricts the nonzero elements to those where $M_L = M_L'$; the second symmetry requires that the density-matrix elements satisfy the equation

$$\rho^{nLM_L}_{n'L'M_L'} = (-1)^{M_L+M_L'} \rho^{nL-M_L}_{n'L'-M_L'} . \quad (1)$$

Coherences between different n levels are generally unobservable in an experiment with a macroscopic length target, macroscopic detection window, or narrow detection bandwidth due to averaging of the rapidly oscillating phases. Thus only density-matrix elements with $n = n'$ are effectively nonzero; this uncouples the different manifolds and leaves $n(n+1)/2$ diagonal elements which represent the collision-produced populations and $n(n^2-1)/6$ off-diagonal elements ($L \neq L'$) which represent coherences between orbital angular momentum levels. For $n = 3$, there are six parameters

$$\rho^{3L\,|M_L|}_{3L\,|M_L|} = \rho^{3L\,|M_L|}_{3L\,|M_L|}$$

for the populations and four complex parameters

$$\rho^{3L\,|M_L|}_{3L'\,|M_L|}$$

for the coherences.

The microwave field interacts with atoms in states which are eigenfunctions of the total Hamiltonian of the hydrogen atom which includes the electron and nuclear spins. The density matrix in this coupled angular momentum basis, $nLJFM_F$, can be found by using Clebsch-Gordan coefficients,

$$\rho^{nLJFM_F}_{nL'J'F'M_F'} = \sum_{M_L,M_S,M_I,M_L',M_S',M_I'} \rho^{nLSIM_LM_SM_L}_{nL'SIM_L'M_S'M_L'} \langle LSM_LM_S \,|\, JM_J\rangle \langle JIM_JM_I \,|\, FM_F\rangle \langle L'SM_L'M_S' \,|\, J'M_J'\rangle \times \langle J'IM_J'M_I' \,|\, F'M_F'\rangle , \quad (2)$$

where

$$M_J = M_L + M_S = M_F - M_I ,$$

$$M_J' = M_L' + M_S' = M_F' - M_I' .$$

Evaluation of Eq. (2) with the previous model for the electron-capture density operator yields the following four types of nonzero density-matrix elements (labeled 1, 2, 3, and 4, respectively):

$$\begin{aligned} &\rho^{nLJFM_F}_{nLJFM_F} , \\ &\rho^{nLJF'M_F}_{nLJFM_F} , \quad F \neq F' \\ &\rho^{nLJ'F'M_F}_{nLJFM_F} , \quad J \neq J' \\ &\rho^{nL'J'F'M_F}_{nLJFM_F} , \quad L \neq L' . \end{aligned} \quad (3)$$

Type-1 elements are diagonal elements describing the populations in this basis; types 2–4 are off-diagonal elements describing coherences induced by the collision-produced coherences between different L levels and the coupling of nuclear and electron spins. It will be shown later that the present experiment is not sensitive to the type-3 or -4 elements. Type-1 and -2 elements are summarized in Tables I and II for the $n = 3$ manifold. Elements with negative M_F can be derived using a relationship obtainable from Eqs. (1) and (2), namely,

$$\rho^{nLJF-M_F}_{nLJF-M_F} = (-1)^{F+F'} \rho^{nLJF'M_F}_{nLJFM_F} . \quad (4)$$

B. Non-electron-capture collisions

So far only single collisions which result in the capture of an electron have been considered. There can also be collisions which cause excitation of a previously formed atom, ionization or quenching of the excited states, decrease of the ion beam due to production of other states, formation of H^-, and elastic scattering. Since the cross section for formation of H^- is small, and the elastic scattering cross section is strongly peaked in the forward direction, we will neglect these two processes. For the present analysis of the remaining collisions in a finite length target, we will examine only the diagonal density-matrix elements or populations. The loss of ions and formation of neutrals can be written

$$\frac{dn_+}{dz} = -\rho\sigma_n n_+ + \rho\sigma_s n_0 , \quad (5a)$$

$$\frac{dn_0}{dz} = \rho\sigma_n n_+ - \rho\sigma_s n_0 , \quad (5b)$$

where σ_n, σ_s are the total capture and stripping cross sections, ρ is the gas density, and n_+, n_0 are the ion and neutral currents. These coupled equations can be solved for a constant density target to yield

$$n_+ = \frac{n_+^0}{\sigma_s+\sigma_n}\{\sigma_s + \sigma_n \exp[-\rho(\sigma_s+\sigma_n)z]\} , \quad (6a)$$

$$n_0 = \frac{n_+^0}{\sigma_s+\sigma_n}\sigma_n\{1 - \exp[-\rho(\sigma_s+\sigma_n)z]\} , \quad (6b)$$

where n_+^0 is the initial ion current and z is the distance into the target.

The growth of an excited-state current n^* will be described by

$$\frac{dn^*}{dz} = \frac{-\gamma n^*}{v} - \rho\sigma_l n^* + \rho\sigma_c n_+ + \rho\sigma_e n_0 , \quad (7)$$

where γ is the spontaneous decay rate, v is the beam speed, and σ_l, σ_c, and σ_e are the cross sections for collisional loss of n^*, charge capture into n^*, and excitation of n_0 to n^* averaged over all the states. Combining Eqs. (6a), (6b), and (7) and solving for n^* yields the excited-state population for a target of length L

TABLE I. Type-1 diagonal density-matrix elements for the $n=3$ manifold of hydrogen. The matrix elements $\rho^{nLJFM_F}_{nLJFM_F}$ are related to the six parameters σ_{nLM_L} describing the partial cross sections for the electron-capture collision.

L	J	F	M_F	$\rho^{nLJFM_F}_{nLJFM_F}$
0	$\frac{1}{2}$	0	0	σ_{300}
0	$\frac{1}{2}$	1	0	σ_{300}
0	$\frac{1}{2}$	1	1	σ_{300}
1	$\frac{1}{2}$	0	0	$\frac{2}{3}\sigma_{311}+\frac{1}{3}\sigma_{310}$
1	$\frac{1}{2}$	1	0	$\frac{2}{3}\sigma_{311}+\frac{1}{3}\sigma_{310}$
1	$\frac{1}{2}$	1	1	$\frac{2}{3}\sigma_{311}+\frac{1}{3}\sigma_{310}$
1	$\frac{3}{2}$	1	0	$\frac{1}{3}\sigma_{311}+\frac{2}{3}\sigma_{310}$
1	$\frac{3}{2}$	1	1	$\frac{5}{6}\sigma_{311}+\frac{1}{6}\sigma_{310}$
1	$\frac{3}{2}$	2	0	$\frac{1}{3}\sigma_{311}+\frac{2}{3}\sigma_{310}$
1	$\frac{3}{2}$	2	1	$\frac{1}{2}\sigma_{311}+\frac{1}{2}\sigma_{310}$
1	$\frac{3}{2}$	2	2	σ_{311}
2	$\frac{3}{2}$	1	0	$\frac{3}{5}\sigma_{321}+\frac{2}{5}\sigma_{320}$
2	$\frac{3}{2}$	1	1	$\frac{3}{5}\sigma_{322}+\frac{3}{10}\sigma_{321}+\frac{1}{10}\sigma_{320}$
2	$\frac{3}{2}$	2	0	$\frac{3}{5}\sigma_{321}+\frac{2}{5}\sigma_{320}$
2	$\frac{3}{2}$	2	1	$\frac{1}{5}\sigma_{322}+\frac{1}{2}\sigma_{321}+\frac{3}{10}\sigma_{320}$
2	$\frac{3}{2}$	2	2	$\frac{4}{5}\sigma_{322}+\frac{1}{5}\sigma_{321}$
2	$\frac{5}{2}$	2	0	$\frac{2}{5}\sigma_{321}+\frac{3}{5}\sigma_{320}$
2	$\frac{5}{2}$	2	1	$\frac{2}{15}\sigma_{322}+\frac{2}{3}\sigma_{321}+\frac{1}{5}\sigma_{320}$
2	$\frac{5}{2}$	2	2	$\frac{13}{15}\sigma_{322}+\frac{2}{15}\sigma_{321}$
2	$\frac{5}{2}$	3	0	$\frac{2}{5}\sigma_{321}+\frac{3}{5}\sigma_{320}$
2	$\frac{5}{2}$	3	1	$\frac{1}{15}\sigma_{322}+\frac{8}{15}\sigma_{321}+\frac{2}{5}\sigma_{320}$
2	$\frac{5}{2}$	3	2	$\frac{1}{3}\sigma_{322}+\frac{2}{3}\sigma_{321}$
2	$\frac{5}{2}$	3	3	σ_{322}

$$n^*=\frac{\rho n^0_+}{\sigma_s+\sigma_n}\left[\frac{\sigma_c\sigma_s+\sigma_e\sigma_n}{\gamma/v+\sigma_l\rho}(1-\exp\{-[\gamma/v+(\sigma_l\rho)]L\})\right.$$
$$\left.+\frac{\sigma_n(\sigma_c-\sigma_e)\{\exp[-\rho(\sigma_s+\sigma_n)L]-\exp[-(\gamma/v+\sigma_l\rho)L]\}}{\gamma/v+\rho\sigma_l-\rho(\sigma_s+\sigma_n)}\right]. \tag{8}$$

Expansion of Eq. (8) in a low-density limit yields

$$n^*=n^0_+(\rho L\sigma_c)\left[\frac{1-\exp(-\gamma L/v)}{\gamma L/v}\right]\left\{1-\left[1-\left[\frac{1}{1-\exp(-\gamma L/v)}-\frac{1}{\gamma L/v}\right]\right]\sigma_l\rho L\right.$$
$$\left.-\sigma_n\rho L\left[1-\frac{\sigma_e}{\sigma_c}\right]\left[\frac{1}{1-\exp(-\gamma L/v)}-\frac{1}{\gamma L/v}\right]+\cdots\right\}. \tag{9}$$

This equation shows that the excited-state current will be linearly dependent on the ion current, target density and length, and the capture cross section if ρL is small. Since the purpose of this experiment was to measure electron-capture cross sections, the target was operated in this low-density regime where the signals depend only on the electron-capture collisions.

TABLE II. Type-2 off-diagonal density-matrix elements for the $n=3$ manifold of hydrogen. The matrix elements $\rho^{nLJFM_F}_{nLJF'M_F}$ are related to the six parameters σ_{nLM_L} describing the partial cross sections for the electron-capture collison.

L	J	F	M_F	L	J	F'	M_F	$\rho^{nLJFM_F}_{nLJF'M_F}$
1	$\frac{3}{2}$	2	1	1	$\frac{3}{2}$	1	1	$(\sqrt{3}/6)(\sigma_{311}-\sigma_{310})$
2	$\frac{3}{2}$	2	1	2	$\frac{3}{2}$	1	1	$(\sqrt{3}/10)(2\sigma_{322}-\sigma_{321}-\sigma_{320})$
2	$\frac{5}{2}$	3	1	2	$\frac{5}{2}$	2	1	$(\sqrt{2}/15)(\sigma_{322}+2\sigma_{321}-3\sigma_{320})$
2	$\frac{5}{2}$	3	2	2	$\frac{5}{2}$	2	2	$(2\sqrt{5}/15)(\sigma_{322}-\sigma_{321})$

C. Free-field evolution

After the formation of the excited-state atom, the atom will transverse a field-free region where the density operator evolves according to the equation

$$\frac{d\hat{\rho}(t)}{dt}=\frac{-1}{i\hbar}[\hat{\rho}(t),H_{\text{atom}}]\ , \tag{10}$$

where H_{atom}, the complex atomic Hamiltonian, is

$$\begin{aligned} &H_{\text{atom}}=H_0+H_1\ , \\ &H_0\,|\,\alpha\rangle=\hbar\omega_a\,|\,\alpha\rangle\ , \\ &H_1\,|\,\alpha\rangle=-\tfrac{1}{2}i\gamma_\alpha\,|\,\alpha\rangle\ . \end{aligned} \tag{11}$$

Solution of Eqs. (10) and (11) provides the evolution of the density matrix in a field-free region,

$$\begin{aligned} &\rho_{\alpha\beta}(t)=\rho_{\alpha\beta}(t_0)\exp[-(i\omega_{\alpha\beta}+\gamma_{\alpha\beta})(t-t_0)]\ , \\ &\omega_{\alpha\beta}=(\omega_\alpha-\omega_\beta)\ , \\ &\gamma_{\alpha\beta}=(\gamma_\alpha+\gamma_\beta)/2\ . \end{aligned} \tag{12}$$

Equations (12) can be used to generalize Eq. (9) to include the coherences. By averaging Eqs. (12) over a target of constant density ρ and length L, the density matrix at the target exit becomes

$$\rho_{\alpha\beta}(L)=\rho_{\alpha\beta}(t_0)\left[\frac{1-\exp[-(i\omega_{\alpha\beta}+\gamma_{\alpha\beta})L/v]}{(i\omega_{\alpha\beta}+\gamma_{\alpha\beta})L/v}\right]\ . \tag{13}$$

The factor in square brackets shows how the exponential decay decreases the populations and coherences in a finite target. The $\omega_{\alpha\beta}L/v$ term in the denominator causes the coherences with large energy separations to average quickly to zero. In particular, the types 3 and 4 and especially the $n\neq n'$ coherences will be greatly reduced. Tables I and II and Eqs. (12) and (13) describe the density matrix in the field-free region after the target as a function of the six $\sigma_{nL\,|M_L|}$ parameters.

D. Atom-microwave field interactions

The most critical part of a MROD experiment is the interaction of the excited-state atoms with the microwave field. The oscillating electric field drives electric dipole transitions which alter or rearrange the excited-state populations. The effect of these transitions are later observed through changes in the visible light emitted in the spontaneous decay of the states. It is necessary to obtain an accurate understanding of the atom-field interaction in order to be able to interpret correctly the observed signals. This analysis will assume that the electric field is a monochromatic microwave field though, in general, other fields such as a laser or constant electric or magnetic field could be utilized to probe the excited-state populations.

The Hamiltonian describing the atom-field interaction can be written as

$$H=H_{\text{atom}}+H_{\text{field}}+H_{\text{int}}\ , \tag{14}$$

where

$$H_{\text{int}}=2\hat{V}\cos(\omega t+\delta)\ , \tag{15a}$$

$$\hat{V}=-\frac{\vec{\mathrm{d}}\cdot\vec{\mathrm{E}}_0}{2}=-\frac{e\vec{\mathrm{r}}\cdot\vec{\mathrm{E}}_0}{2}\ , \tag{15b}$$

H_{atom} is the Hamiltonian described in Eq. (11), and H_{field} is the Hamiltonian describing the radio-frequency field which we treat classically due to the large number of photons. H_{int} describes the interaction of this external field of amplitude $\vec{\mathrm{E}}_0$ with the atomic electric dipole moment $\vec{\mathrm{d}}$. Initially we will assume that all the atoms enter the interaction region at the same phase δ and that the field has a constant magnitude and direction. The axis of quantization $\vec{z}$ will always be chosen to be along the radio-frequency electric field and the density operator in this coordinate system will be calculated by using the appropriate rotation operators. Later we will generalize the

results to describe the situation where the atoms enter at random phases and the amplitude and direction of the field varies spatially.

Instead of solving for the evolution of the density matrix directly, it is mathematically more convenient to solve for the state amplitude $a_i(t)$ and use this solution to calculate the density matrix, $\rho_{ij}(t)=a_i(t)a_i^*(t)$. From the Schrödinger equation, the following set of coupled equations are obtained for the amplitude:

$$\frac{da_\alpha(t)}{dt}=-\left[i\omega_\alpha+\frac{\gamma_\alpha}{2}\right]a_\alpha(t) -i\sum_{k=1}^{n}V_{\alpha k}a_k(t)(e^{i(\omega t+\delta)}+e^{-i(\omega t+\delta)}) , \tag{16}$$

where $V_{\alpha k}=\langle\alpha\,|\,V\,|\,k\rangle$ is the dipole matrix element. Evaluation of these matrix elements in hydrogen for the case in which the field is along the z axis yields

$$\langle nL_1J_1F_1M_1\,|\,z\,|\,nL_2J_2F_2M_2\rangle=(-1)^{J_1+J_2-M_1}\tfrac{3}{2}n((2F_1+1)(2F_2+1)(2J_1+1)(2J_2+1) \times(2L_1+1)(2L_2+1)\{n^2-[\max(L_1,L_2)]^2\})^{1/2} \times\begin{Bmatrix}J_1 & J_2 & 1\\ F_2 & F_1 & \frac{1}{2}\end{Bmatrix}\begin{Bmatrix}L_1 & L_2 & 1\\ J_2 & J_1 & \frac{1}{2}\end{Bmatrix}\begin{bmatrix}F_2 & 1 & F_1\\ M_2 & 0 & -M_1\end{bmatrix}\begin{bmatrix}L_1 & 1 & L_2\\ 0 & 0 & 0\end{bmatrix}a_0 , \tag{17}$$

where the large parentheses and the large curly brackets denote, respectively, the usual 3-J and 6-J symbols. The solution to Eq. (16) can be written in matrix notation,

$$\underline{A}(t)=\underline{M}(t,t_0,\omega,\delta,E_0)\underline{A}(t_0) , \tag{18}$$

where $\underline{A}(t)$ is a column vector of the state amplitudes and $\underline{M}(t,t_0,\omega,\delta,E_0)$ is the matrix describing the affect of the microwave field on the excited states. In terms of $\underline{M}$ the time development of the density matrix is given by

$$\rho_{\alpha\beta}(t)=M_{\alpha k}(t,t_0,\omega,\delta,E_0)\rho_{kj}(t_0)M^*_{\beta j}(t,t_0,\omega,\delta,E_0) . \tag{19}$$

Equation (16) cannot be solved analytically without some approximations. The equation is first transformed to the interaction representation

$$a_\alpha=b_\alpha e^{-i\omega_\alpha t} .$$

All the remaining terms containing time-dependent exponentials are then assumed to have no net effect and are set equal to zero. This approximation is a combination of the usual rotating field approximation which neglects antiresonant terms and the neglect of states which are far from resonance with the applied field. These two effects will produce small line-shape asymmetries which can be important in precision line center studies but are negligible in this experiment. The coupled equations then separate into a group of uncoupled states which evolve according to Eq. (12) and a small number of groups of states which are coupled by the microwave field. Evaluation of the coupling matrix using Eq. (17) leads to three basic types of transitions, those involving coupling of 2, 3, or 4 states. Figure 3 shows the allowed $\Delta M=0$ electric dipole transitions in the $n=3$ manifold with the dipole matrix elements and energy separations. This uncoupling of states is one of the advantages of using the MROD technique to probe the excited-state populations. The signal at any particular frequency will depend on only a small number of states within the manifold; this greatly simplifies the analysis.

Since the resonances couple at most four states at one time, it is possible to derive analytic solutions to these equations. The solutions for 2, 3, or 4 coupled levels have been derived previously.[24–26] There are some errors in the published solutions. Correct expressions have been given by one of the authors.[27] Since the solutions are analytic their accuracy depends only on neglected nonresonant terms which contribute less than 1 part in 10^3 to the peak signal height. The complete matrix $\underline{M}$ for the whole manifold will be given by appropriate combinations of these solutions.

In general, the field will vary spatially in both amplitude and direction. This generalized problem can be solved by subdividing the interaction region into N segments where N is chosen sufficiently large so that to a good approximation the field can be assumed to be of uniform polarization and magnitude within each segment. The evolution matrix in the interaction region can be written as

$$\underline{M}(t,t_0,\omega,\delta,\vec{\mathrm{E}})=\prod_{k=1}^{N}\underline{M}(t_0+kT,t_0+(k-1)T,\omega, \delta+(k-1)\omega T,\vec{\mathrm{E}}_k)\hat{R}(\theta_k-\theta_{k-1}) , \tag{20}$$

where T is the time spent in each region and $R(\theta_k-\theta_{k-1})$ is the rotation operator from the field direction θ_{k-1} to θ_k (θ_0 is the beam direction). The effect of this changing field amplitude or polarization is very important for determining the experimental line shapes. If either is changing rapidly with a distance scale comparable to vNT, then there can be significant line broadening or even oscillatory shapes such as found in Ramsey's separated oscillatory field experiments. These effects are properly taken into account by the simulation technique and are not a major source of uncertainty in the analysis of the data. To describe the experiments where the atoms enter at random times, Eq. (20) is averaged over the phase δ of the microwave field. This average leads to an uncoupling of the first three types of density-matrix elements from the type-4 elements of mixed parity. Instead of averaging Eq. (20) directly, the evolution of the first three types of density-matrix elements can equivalently be found by evaluation of $\underline{M}$ at one phase ($\delta=0$) and then neglecting mixed parity matrix elements.

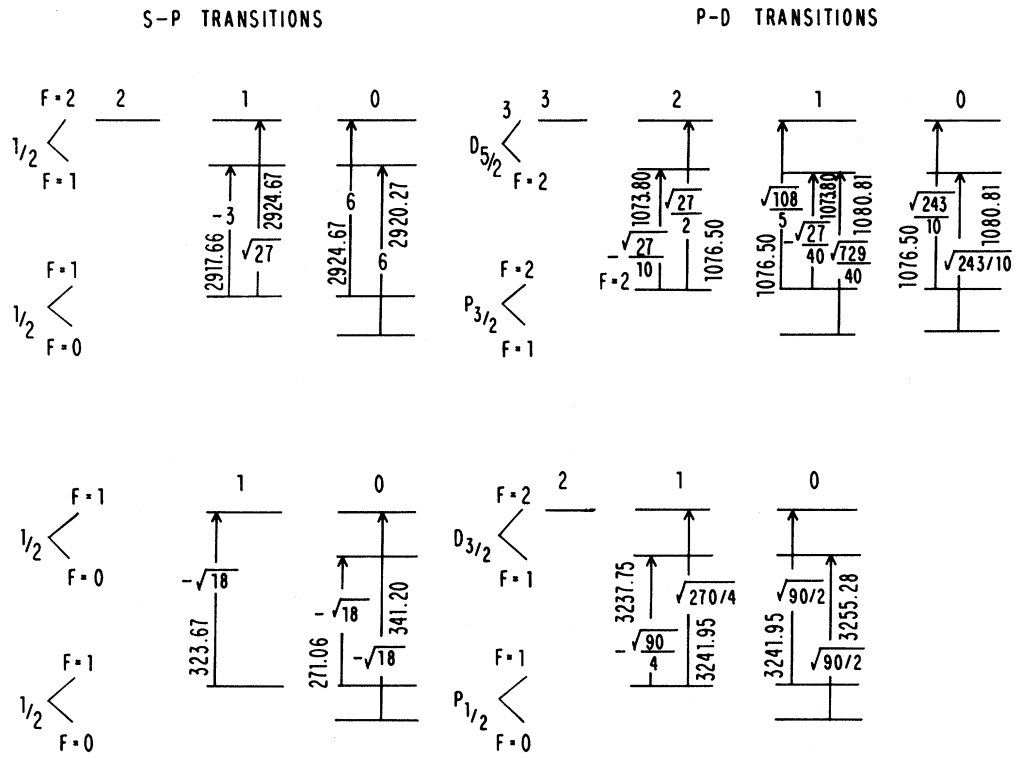

FIG. 3. Allowed $M=0$ electric dipole transitions for each of the M_F states in the $n=3$ manifold of atomic hydrogen. The horizontal numbers are the electric dipole matrix elements in units of the Bohr radius; the vertical numbers are the energy separations in MHz.

E. Optical detection

After the microwave interaction region, the excited-state atoms transverse a field-free region where their evolution is described by Eq. (12). The atoms then enter the detection region where an optical detector such as a photomultiplier with a suitable polarizer and filter is used to monitor the spontaneous emission of light. The probability for detecting photons from a particular atomic level depends on the lifetime of the level, the velocity of the beam, the geometry of the observation window, the transmission of the filter polarizer combination, and the quantum efficiency of the photomultiplier. A schematic diagram of the detector geometry utilized in this experiment is shown in Fig. 4. A coordinate system is used in which the z axis is along the beam and the x axis is parallel to the axis of the detector.

The probability W for detecting a photon from an atom is[25,28]

$$W=\frac{e^2\omega^3}{\hbar c^3}\int_{\Omega_0}d\Omega\int_0^\infty dz'\sum_{f,i,i',\lambda,\lambda'}\epsilon_{\lambda\lambda'}(\hat{p},\hat{k},z')\langle f\,|\,\vec{r}\cdot\hat{e}^*_{\lambda'}\,|\,i\rangle\rho_{ii'}(0)\langle i'\,|\,\vec{r}\cdot\hat{e}_\lambda\,|\,f\rangle\exp[-(i\omega_{ii'}+\gamma_{ii'})t']\,, \tag{21}$$

where

$$t'=z'/v\,.$$

In this expression $\underline{\epsilon}(\hat{p},\hat{k},z')$ is the efficiency matrix for detection of a linearly polarized photon emitted at the point z' with a propagation direction given by the unit vector $\hat{k}$ and with the electric field polarized along the direction given by the unit vector $\hat{p}$. The angular distribution of the radiation is determined by the projection of the electron coordinate operator on the unit polarization vector, $\hat{e}_\lambda(k)$. For a general direction of propagation $\hat{k}$ these vectors are given in terms of the unit vectors $\hat{e}_\nu$ defined by

$$(\hat{e}_\nu)=(\hat{e}_{+1},\hat{e}_0,\hat{e}_{-1})=\left[-\frac{\hat{x}+i\hat{y}}{\sqrt{2}},\hat{z},\frac{\hat{x}-i\hat{y}}{\sqrt{2}}\right] \tag{22}$$

by the equation

$$\hat{e}_\lambda(k)=\sum_\nu \mathscr{D}^1_{\nu\lambda}(\hat{k})\hat{e}_\nu\,. \tag{23}$$

Here $\hat{x}$, $\hat{y}$, and $\hat{z}$ denote unit vectors along the x, y, and z axis, respectively, and the argument $\hat{k}$ of the rotation matrix $\underline{\mathscr{D}}^1(k)$ is the set of Euler angles $(\phi_k,\theta_k,0)$ through which the $\hat{z}$ is rotated into the $\hat{k}$ axis. We can accordingly write W as

$$W=\frac{e^2\omega^2}{\hbar c^3}\int_{\Omega_0}d\Omega\int_0^\infty dz'\sum_{f,i,i',\nu\nu'}A_{\nu\nu'}\langle f\mid\vec{r}\cdot\hat{e}_\nu^*\mid i\rangle\langle i'\mid\vec{r}\cdot\hat{e}_\nu\mid f\rangle\rho_{ii'}(z')\ , \tag{24}$$

where

$$A_{\nu\nu'}=\sum_{\lambda,\lambda'}\epsilon_{\lambda\lambda'}(\hat{p},\hat{k},z')\mathscr{D}^{1*}_{\nu\lambda'}(\hat{k})\mathscr{D}^{1}_{\nu\lambda}(\hat{k})\ .$$

Figure 5 shows the relationship between the several vectors together with the linear polarization vector axes used to describe the photon emitted with propagation vector $\hat{k}$. Evaluation of the matrix elements in the spherical basis ($\hat{e}_\nu$) yields

$$\langle nLJFM\mid\vec{r}\cdot\hat{e}_\nu\mid n'L'J'F'M'\rangle=(-1)^{F-M}\begin{pmatrix}F&1&F'\\-M&\nu&M'\end{pmatrix}$$
$$\times(-1)^{J+J'+F'+1}[(2F+1)(2F'+1)(2J+1)(2J'+1)(2L+1)(2L'+1)]^{1/2}$$
$$\times\begin{Bmatrix}J&F&\frac{1}{2}\\F'&J'&1\end{Bmatrix}\begin{Bmatrix}L&J&\frac{1}{2}\\J'&L'&1\end{Bmatrix}\begin{pmatrix}L&1&L'\\0&0&0\end{pmatrix}R_{nL}^{n'L'}\ , \tag{25}$$

where $R_{nL}^{n'L'}=\langle nL\mid r\mid n'L'\rangle$. The selection rules for spontaneous emission are determined by the properties of the 3-J and 6-J expressions,

$$|L_i-L_f|=1\ , \tag{26a}$$
$$|L_i'-L_f|=1\ , \tag{26b}$$
$$|J_i-J_f|=0,1\ , \tag{26c}$$
$$|J_i'-J_f|=0,1\ , \tag{26d}$$
$$|F_i-F_f|=0,1\ , \tag{26e}$$
$$|F_i'-F_f|=0,1\ , \tag{26f}$$
$$M_i-M_f=\nu'\ , \tag{26g}$$
$$M_i'-M_f=\nu\ . \tag{26h}$$

Equations (26a) and (26b) make the mixed parity density-matrix elements unobservable. Since the microwave field does not couple these type-4 elements with the observable same parity elements (types 1–3), this experiment will not be sensitive to the mixed parity cross sections where $L\neq L'$. These cross sections can be detected if there is an additional field (i.e., a static electric field) which mixes the states. The integration axes z' in Eq. (21) decreases the sensitivity to the spin-induced coherences (type-2 and -3 elements) due to the averaging of the phases. For the detector geometry used in this experiment, the electron–spin-induced coherences ($J\neq J'$) contribute negligibly to the signal and only the nuclear–spin-induced coherences ($F\neq F'$) and the diagonal matrix elements were retained in the data analysis.

The efficiency matrix for the detection of a photon with linear polarization $\hat{p}$ can be written in the form

$$\epsilon_{\lambda\lambda'}=D(\hat{k},z)P_{\lambda\lambda'}(\hat{p},\hat{k},z)F(\hat{k},z)\ . \tag{27}$$

The F, $P_{\lambda\lambda'}$, and D describe, respectively, the action of the

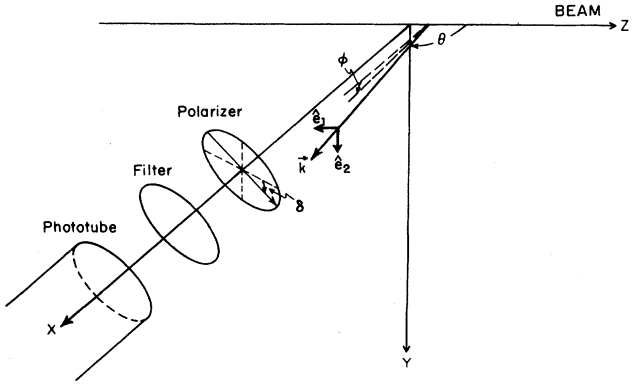

FIG. 4. Diagram showing the detector geometry. The angle between the transmission axis of the polarizer and the beam direction is δ. The orientation of the unit vectors $\hat{e}_1$ and $\hat{e}_2$ in terms of which the polarization of the photon is described are depicted with greater detail in Fig. 5.

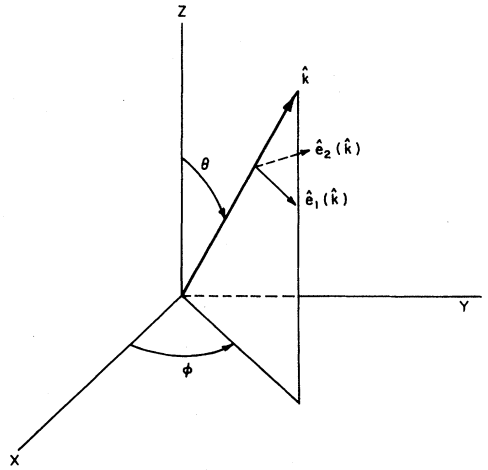

FIG. 5. Diagram showing the coordinates used to describe the direction of propagation of the photon and the unit vectors $\hat{e}_1(\hat{k})$ and $\hat{e}_2(\hat{k})$ in terms of which the polarization of the emitted photon is described.

filter, polarizer, and detector on photons emitted at z with propagation vector $\hat{k}$ and the polarizer set to transmit photons with the polarization vector in the direction $\hat{p}$.

The filter used in this experiment is a Balmer-α narrow-band dielectric interference filter which resolves the $n=3$ manifold but not individual levels within this manifold. The transmission efficiency of the filter can be written as

$$F(z,\hat{k})=T_f(\omega(\theta),\omega_c(\theta),\Delta\omega) , \tag{28}$$

where

$$\omega(\theta)=\left[\frac{1+(v/c)\cos\theta}{[1-(v/c)^2]^{1/2}}\right]\omega_0 , \tag{29}$$

$$\omega_c(\theta)=\omega_0\frac{n}{(n^2-\cos^2\theta)^{1/2}} . \tag{30}$$

Here $\omega(\theta)$ is the angular frequency for the emitted light in the laboratory coordinate system, $\omega_c(\theta)$ is the center of the pass band for the interference filter corrected for angular effects, v is the velocity of the beam, n is the effective index of refraction for the filter, and $\Delta\omega$ is the bandwidth for the filter. The function T_f has to be determined experimentally. Owing to the angular dependence there is a limited detection cone; for a 6536-Å filter with a full width at half maximum (FWHM) of 100 Å detecting radiation from 49-keV hydrogen atoms, the cone is limited to 30° FWHM and is slightly asymmetric.

For light at normal incidence, and a polarizer with complete extinction for the orthogonal polarization, the transmission efficiency of the polarizer is given by

$$P_{\lambda\lambda'}(\hat{p},\hat{k},z)=T_p\begin{bmatrix}\frac{1}{2} & -\frac{1}{2}e^{-2i\delta}\\ -\frac{1}{2}e^{2i\delta} & \frac{1}{2}\end{bmatrix} , \tag{31}$$

where T_p is the experimentally measured transmission efficiency for the polarizer and δ is the angle between the transmission axis of the polarizer and the $\hat{e}_1$ axis depicted in Figs. 4 and 5. Corrections to Eq. (31) due to oblique incidence[25] are small (1% for a 60° FWHM cone) and not important for this experiment. The detector function $D(\hat{k},z)$ is weakly dependent on the wavelength, polarization, and photon direction and must be determined experimentally.

F. Theoretical signal

The signal is defined as the fractional decrease in the observed light when the microwave field is switched on through the equation

$$S(\omega,\vec{E},\delta)=[N(0,\vec{0},\delta)-N(\omega,\vec{E},\delta)]/N(0,\vec{0},\delta) , \tag{32}$$

where $N(0,\vec{0},\delta)$ is the count rate in the absence of the microwave field, $N(\omega,\vec{E},\delta)$ is the count rate with a microwave field with an angular frequency ω and a field strength $\vec{E}$, and δ is the angle between the transmission axis of the polarizer and the beam axis. This signal can be calculated using the previous results and expressed in the form

$$S(\omega,\vec{E}_0,\delta)=\sum_{L,M_L} A_{L\,|M_L|}(\omega,\vec{E}_0,\delta)\sigma_{nL\,|M_L|} , \tag{33}$$

where the functions $A_{L\,|M_L|}$ relate the signals to the partial capture cross sections. The partial cross sections are the only free parameters to be determined from the signals. Even though the cross sections uniquely determine the signals it will not in general be possible to invert the matrix and unambiguously determine the cross sections from the signals. Since each group of resonances (e.g., $P_{3/2}$-$D_{5/2}$) consists of several unresolved hyperfine components, the measurement of each resonance group will provide a good determination of one linear combination of cross sections and a poor determination of other combinations. Thus one experimental configuration (e.g., microwave electric field and optical polarizer perpendicular to the beam axis) will determine four linear combinations of cross sections using the $S_{1/2}$-$P_{1/2}$, $S_{1/2}$-$P_{3/2}$, $P_{1/2}$-$D_{3/2}$, and $P_{3/2}$-$D_{5/2}$ transitions. Since there are six partial cross sections $\sigma_{3L\,|M_L|}$ describing the $n=3$ manifold, it will not be possible to determine the individual cross sections from a single experimental configuration. By using different configurations such as with both the radio-frequency field and the optical polarizer perpendicular to the beam, one can obtain signals which depend on a different linear combination of the populations. By utilizing the four combinations of radio-frequency field polarization and polarizer transmission axis either parallel or perpendicular to the beam axis, it is possible to determine unambiguously the six independent partial cross sections.

So far the analysis that led to Eq. (33) has only considered states within the manifold of interest ($n=3$) and has neglected upper manifolds which can cascade down to the states of interest. The cascades can affect the MROD signal via two paths. First, the populations in the upper manifolds can decay into the $n=3$ manifold and add to a states's population so that it will no longer be simply due to electron capture. The ratio $R(t)$ of this cascade-induced population and the initial electron-capture population of a particular state (neglecting repopulation of the cascading state) can be expressed as

$$R(t)=\sum_{i'}\frac{\gamma_{ii'}p_{i'}(0)}{p_i(0)}\frac{e^{(\gamma_i-\gamma_{i'})t}-1}{\gamma_i-\gamma_{i'}} , \tag{34}$$

where $\gamma_{ii'}$ is the decay rate from the cascade state i' to the $n=3$ state i, γ_i and $\gamma_{i'}$ are the total decay rates, $p_i(0)$ and $p_{i'}(0)$ are the initial populations, and t is the time since the collision. The MROD signal will be sensitive only to the populations at the interaction region so that only cascade repopulation between the target and interaction region will be important. In the limit $t\to 0$,

$$R(t)\to\sum_{i'}\frac{p_{i'}(0)}{p_i(0)}\gamma_{ii'}t . \tag{35}$$

This shows that cascade repopulation can be minimized by keeping the target to interaction distance d short as compared to $v/\gamma_{ii'}$. Cascades can also affect the observed signals if the microwave field is resonant with a transition in a higher manifold which is detected in the subsequent

decay through the $n=3$ manifold. The two groups of $J=\frac{1}{2}$-$J=\frac{3}{2}$ transitions will be free from these cascades and the $J=\frac{3}{2}$-$J=\frac{5}{2}$ resonances will have only a small overlapping signal from the $n=4$, $J=\frac{1}{2}$-$J=\frac{3}{2}$ resonances. Since the experiment can resolve the resonances, the residual overlap can be subtracted. The $n=3$, $^2S_{1/2}$-$^2P_{1/2}$ Lamb-shift resonance will be strongly affected by cascading signals and therefore cannot be used in the analysis without knowledge of populations in the higher manifolds. It is still possible to determine uniquely the individual cross sections utilizing only the upper three resonances. Thus cascades will not be important in a short geometry after corrections are made for small residual overlapping signals.

IV. APPARATUS

A schematic diagram of the fast-beam apparatus is shown in Fig. 6. The proton beam is produced in a commerical radio-frequency ion source (Accelerators Inc. #1). The protons are extracted, focused, and then accelerated down a high-voltage column. After leaving the accelerator, the beam passes through an electrostatic quadrupole, 30° horizontal bending magnet, another quadrupole, and a pair of balanced vertical deflection plates. This arrangement focuses the beam, separates protons from the molecular ions H_2^+,H_3^+, and steers the beam. Immediately prior to the measurement region, the beam passes through two 1.6-mm aperatures spaced 50 cm apart which collimate the beam to 3.2 mrad. This collimation was found necessary so that the protons would traverse the beam line without striking any surface; this eliminated the potentially large alteration of the signals due to complex beam-surface interactions. The signals were quite unreproducible if the beam was allowed to strike surfaces in the measurement region. All the components of the experiment were optically aligned to about 0.3 mm with a surveyors level. The proton current entering the measurement region was typically 3–4 μA. The beam energy was determined independently from the accelerating potentials and from the bending magnetic field. All the data described in this paper was measured with an incident proton energy of 49.0(5) keV.

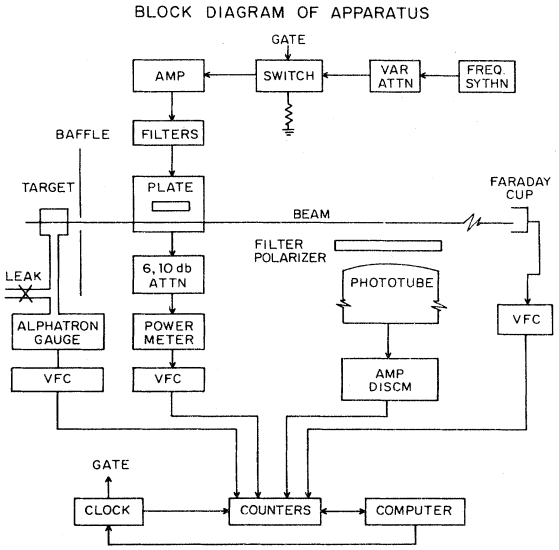

FIG. 6. Block diagram of the fast-beam apparatus showing the method used to record the data.

The target where the fast protons undergo electron-capture collisions with gas molecules used a cross beam configuration. Either molecular nitrogen or hydrogen was leaked through a glass capillary array disk which produced a collimated gas flow directed into a vacuum pump. The glass disk was mounted in a grounded holder 0.23 cm from the beam so that possible stray electric fields at the beam axis would be minimized. No distortions of the signals which could be attributed to charge buildup in the charge exchange cell were observed. The beam traversed the target which was carefully baffled so that there would be negligible gas leakage into the surrounding regions. This design produced a localized target of constant density with a length of 1.27 cm. The operational modes of the target were either at zero gas pressure (to measure backgrounds) or at a nominal pressure as measured by an alphatron gauge located on the input gas flow line. The density at the beam axis was determined by two independent methods. From the measured pressure at the gas inlet and calculations of the vacuum conductance of the intervening tubing, the nominal gas pressure corresponded to an effective beam axis pressure of $1.6(6)\times10^{-4}$ Torr. The knowledge of these pressures is not important for relative cross sections but is required to determine the magnitude of the cross sections. For this calculation we used the average value of $1.7(5)\times10^{-4}$ Torr for nitrogen and $1.4(5)\times10^{-4}$ Torr for hydrogen. These target densities neutralized approximately 0.3% of the incident proton beam. Since the purpose of the experiment was to measure the electron-capture cross sections, the gas density had to be sufficiently small so that the signals depended linearly on the pressure. The measurement of the number of excited-state atoms participating in any particular resonance as a function of target pressure was found to be linear to within a few percent at the above gas density. Thus we assumed that the signals were purely due to single electron-capture collisions.

The microwave interaction region utilized was a precision TEM transmission line constructed as shown in Fig. 7. The relative dimensions of the rectangular coaxial line were chosen so that the impedance is close to 50 Ω and the absolute dimensions were chosen so that only the TEM mode would propagate without excessive broadening of the resonance line shapes due to a small transit time. The atomic beam could enter the interaction region either parallel or perpendicular to the center conductor by rotation of the two connecting round coaxial transmission lines. This design produced an electric field polarization which could be chosen to be either primarily perpendicular or parallel to the beam axis. The beam entered the interaction region through longitudinal slots which removed the microwave discontinuities from the beam axis and allowed sufficient pumping of the interior.

The microwave source was an Ailtech 3600 frequency

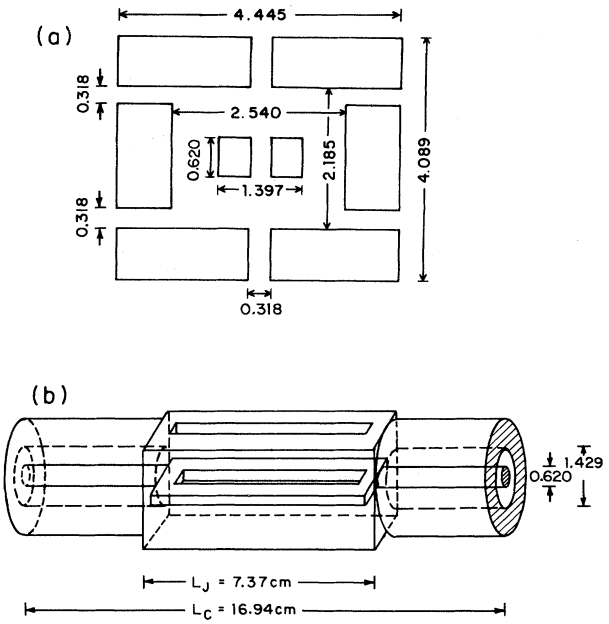

FIG. 7. Drawing showing the construction of the microwave interaction region. All the dimensions are in centimeters. (a) shows a cross section through the center of the microwave interaction region. (b) gives a perspective view showing the construction of the central conductor. To simplify the drawing the parts in the side are not shown. The 0.620-cm dimension is the outer diameter of the center conductor for the coaxial line entrance to the microwave interaction region.

synthesizer capable of producing 10 mW from 1—2000 MHz with several Hz linewidth and resolution. The output power was regulated with a variable attenuator and fed to a switch. The solid-state switch was controlled by the data acquisition system and could be switched in a microsecond with 55 dB isolation into either a dummy load or a suitable amplifier. The microwaves were amplified with either a solid-state amplifier covering 0—1 GHz or one of the two traveling wave tube amplifiers covering 1—2 and 2—4 GHz with a frequency doubler preceding the latter. For every frequency, at least one high-pass and one low-pass filter was used to ensure spectral purity to 50 dB or better. This power was fed through the interaction region to a 6-dB GR-900 attenuator and 10-dB Narda 707C attenuator with the transmitted power measured with a Hewlett-Packard 432A power meter using a thermistor sensing head. All the data reported in this paper was obtained with a power meter reading of 6 or 10 mW (nominally 240 or 400 mW at the beam axis). This power was sufficient to obtain strong signals without excessive power broadening or multiphoton effects. The power broadening is included in the theoretical calculation; its major effect is to increase the width of the individual hyperfine components and thus the degree to which they overlap.

In order to perform the calculations necessary to derive the cross sections, the field shape and amplitude must be known on the beam axis. The field shape of the TEM

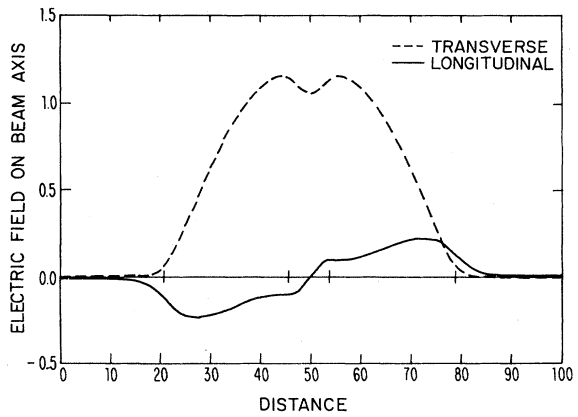

FIG. 8. Plot of the magnitude of the two components of the microwave electric field along the beam axis for the configuration in which the field is perpendicular to the beam axis.

mode was determined by solving Laplace's equation with a relaxation method on a grid size of 300×300 and the resultant on axis fields are shown in Figs. 8 and 9 for the two configurations used in the experiment. The experiment was performed with a constant power as indicated on the microwave power meter. The actual microwave power at the beam will be a function of this transmitted power, the reflections of the transmission line junctions and external components, and the frequency variations of the attenuators and power meter response. By carefully determining each of these corrections, the power at the beam as a function of frequency for a constant meter indication was determined. It is shown in Fig. 10. This power curve was used to correct the raw data so that all the data could be compared at the same effective beam axis power.

The optical detector was a RCA 8852 photomultiplier which was cooled to $-20\,^{\circ}C$ by a thermoelectric refrigerator to reduce the dark noise. Between the photomultiplier and atomic beam, an interference filter with a FWHM pass band of 100 Å and a linear polarizer were mounted in

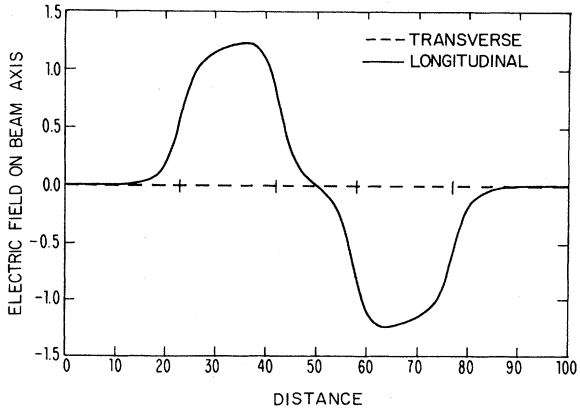

FIG. 9. Plot of the magnitude of the two components of the microwave electric field along the beam axis for the configuration in which the field is along the beam axis.

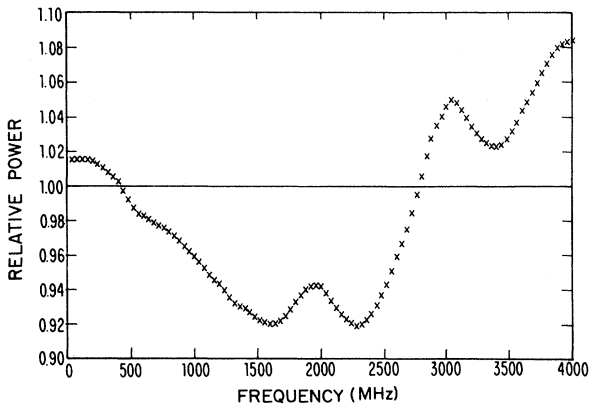

FIG. 10. Plot of the relative microwave power at the beam as a function of frequency for constant microwave power as measured by the power meter.

a rototable disk which allowed the selection of the desired polarization of the Balmer-α light. The output of the photomultiplier was amplified and discriminated to allow pulse counting with a typical rate of 5 kHz at the typical beam currents and target pressures previously mentioned. The overall detection efficiency was determined from the calculated solid angle of the detection window and the manufacturer's specifications of the optical components to be $\epsilon_{\rm det}=(2.5\pm1.1)\times10^{-4}$. The polarization dependence of this detection efficiency was found by measuring the $S_{1/2}$-$P_{1/2}$ resonance in a geometry where over 99% of the observed light arises from the S state decay which is unpolarized. This measurement gave the result $\epsilon_{||}/\epsilon_{\perp}=0.9695(37)$ for the ratio of detection efficiencies when the polarizer transmission axis is parallel or perpendicular to the beam axis.

At the end of the beam line, a Faraday cup with electron suppressor was used to monitor the proton current. The apparatus was pumped by several large diffusion pumps with a total rated pumping speed of 5000 l/sec which achieved a pressure of 3×10^{-7} Torr throughout the measurement region and 8×10^{-7} Torr in the remainder of the apparatus. All materials used in the apparatus were selected to be nonmagnetic and three large mutually orthogonal pairs of Helmholtz coils were used to reduce the earth's magnetic field at the measurement region to less than 2×10^{-2} G. Several procedures were utilized to reduce stray electric fields. As mentioned earlier, the beam was carefully collimated and aligned to avoid beam-surface interactions which can neutralize the beam and release copious quantities of electrons. All internal vacuum vessel walls were made of conductive materials or shielded with screens to avoid the buildup of charge. The diffusion pumps were trapped with liquid N_2 and used DC 705 pump oil to reduce backstreaming to a minimum. Finally, the beam current was restricted to 4 μA to reduce space charge fields to less than 0.016 V/cm. This small electric field and the 20-mg residual magnetic field were believed to be the only stray fields in the apparatus.

V. RESULTS

A. Data-taking procedure

The outputs of the alphatron gauge (ρ), microwave power meter (P), and Faraday cup (I) were digitized using voltage to frequency converters and recorded along with the photomultiplier pulses (N) by a bank of computer-controlled counters. One 64-sec data point consisted of recording these four count rates for each state of the microwave field as it was switched on and off at a 62.5-Hz rate. The photon count rate N was corrected for short-term variations in the incident proton beam intensity by dividing by I and small deviations in the microwave power P from the nominal value P_0 were reduced by multiplying by the normalization factor P_0/P. To improve the signal-to-noise ratio and eliminate counts arising from the residual gas (5—10% of total counts), the signal at each frequency was calculated from three data points obtained at the nominal gas density ρ_0 and three points obtained at zero density. With the use of the notation $(N/I)_{(\rho,P)}$ to represent the average of the three values of N/I obtained at a gas density ρ and microwave power P, the experimental signal S was defined as

$$S=\frac{[(N/I)_{(\rho_0,0)}-(N/I)_{(\rho_0,P_0)}]-[(N/I)_{(0,0)}-(N/I)_{(0,P_0)}]}{(N/I)_{(\rho_0,0)}-(N/I)_{(0,0)}}\,. \tag{36}$$

The numerator is the change in the photon count rate per unit beam due to the microwave field and dependent on the gas density in the target. The denominator is the microwave off photon count rate per unit beam due to only the gas in the target. This form reduces variations in the signal due to small drifts in the detection efficiency, target density, and background gas pressure. The signal defined in this manner was found to be reproducible over several months.

The signal was measured in the experimental configurations where the microwave field polarization was primarily parallel or perpendicular and the optical polarizer transmission axis was parallel or perpendicular to the beam axis. Since the rectangular coax line was located off center between the rotating cylinders, the configuration with the parallel electric field could be obtained with the interaction region being either closer to or further from the target so that data were measured in six different configurations. With nitrogen as the target gas, the signal was measured every 20 MHz from 20 to 4000 MHz to produce panoramic linescans for the six configurations. These panoramic linescans were labeled $N1$. Figures 11 and 12 show the linescans obtained in the configurations where the electric field was, respectively, perpendicular and parallel to the beam and the optical polarizer was perpendicular to the beam. The line shapes obtained in the

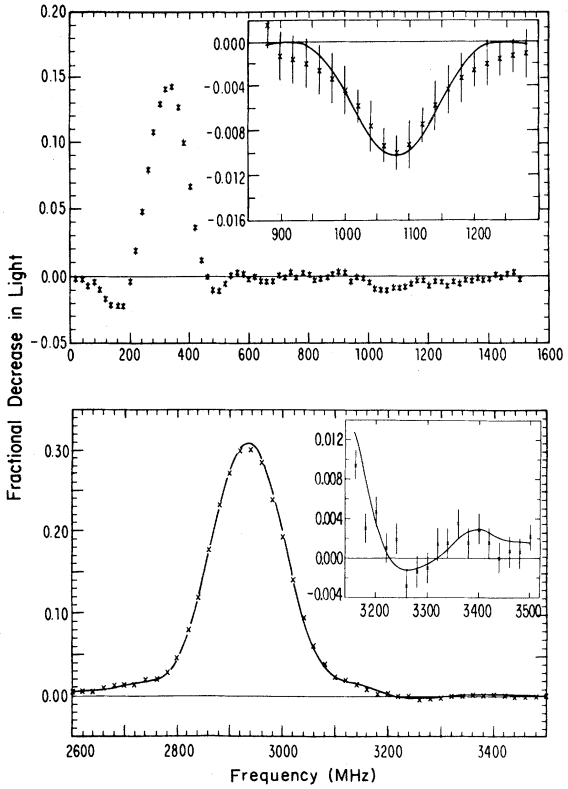

FIG. 11. Plot of the signals as a function of frequency for the configuration in which the microwave electric field is perpendicular to the direction of the beam and the transmission axis of the polarizer is perpendicular to the direction of the beam. The solid curves show the fit to the data used to determine the partial cross sections.

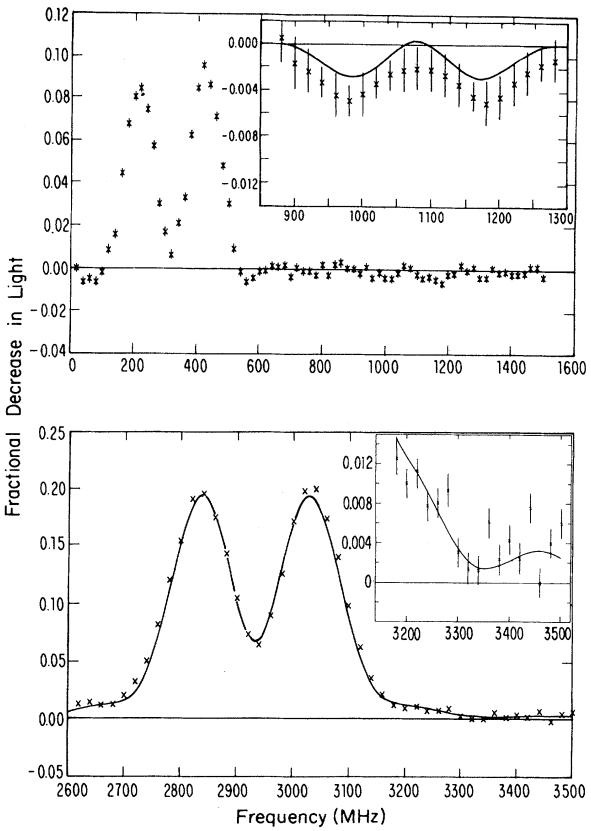

FIG. 12. Plot of the signals as a function of frequency for the configuration in which the microwave electric field is parallel to the direction of the beam and the transmission axis of the polarizer is perpendicular to the beam. The solid curves show the fit to the data used to determine the partial cross sections.

perpendicular electric field scans have the usual Lorentzian line shape while the parallel electric field scans have unusual line shapes which appear as two Lorentzian-type curves evenly spaced around the resonance center. The later curves arise from the oscillatory electric field envelope shown in Fig. 8. The Fourier components of this envelope lead to two resonance curves centered at $f_0 \pm v/L$, where $2L$ is the distance between the two points where the field has its maximum value and v is the velocity of the beam. These data show the importance of the electric field envelope in determining the experimental line shape. Both configurations show the expected $n=3$ electric dipole transitions at 320, 1080, 2940, and 3240 MHz with the additional small cascade resonances at 1240, 1360, and below 600 MHz.

The data contained in these six full scans required the equivalent of 78 h of continuous data accumulation. Since the line-shape function can be accurately calculated, the information about the electron-capture cross sections can be obtained from a few points at each resonance. The remaining data sets were measured only at the resonance peaks (two frequencies per resonance) of the $n=3$ transitions and the $n=4$, $J=\frac{1}{2}$-$J=\frac{3}{2}$ cascades. This provided sufficient data to determine the cross sections in less than eight continuous hours. Two sets of data labeled $N2$ and $N3$ were measured with nitrogen as the target at a nominal microwave power of 240 and 400 mW, respectively, and one set of data $H1$ was measured with molecular hydrogen as the target at a power of 400 mW. All measurements were performed with a 49-keV incident proton beam. These sets of data provide three independent determinations of the $n=3$ electron-capture cross sections for a nitrogen target and one determination of the hydrogen target cross sections.

B. Systematic corrections

Several small systematic corrections were applied to the signals so that all the data could be analyzed under equivalent experimental conditions. The signal defined by Eq. (36) requires a normalization to the total emitted photon count rate N which can be different for the two optical polarizations. The photon count rate $N\epsilon$ was measured several times with the resulting ratio $N_{||}\epsilon_{||}/N_{\perp}\epsilon_{\perp}$ equal to 0.9428(8) for the nitrogen target and to 0.9791(65) for the hydrogen target. When combined with the detection efficiency ratio $\epsilon_{||}/\epsilon_{\perp}$ described earlier these data yield a ratio $N_{||}/N_{\perp}$ equal to 0.9728(38) for nitrogen and

1.0010(38) for hydrogen. This result shows that the emitted light is slightly polarized perpendicular to the beam axis for nitrogen and unpolarized for hydrogen. The data obtained with the parallel optical polarization were multiplied by these ratios.

The signals were measured at the same nominal power as measured by the power meter. In order to compare all the data obtained at different frequencies at the same microwave electric field, a linear power correction was applied using the data shown in Fig. 10. Cascades systematically altered the signals by the repopulation of the levels and creation of overlapping signals. In the configuration with the longest target to interaction region distance, the transit time was 12 nsec. For this situation Eq. (34) predicts that 2%, 4%, 8%, and 15%, respectively, of the original $4S$, $4P$, $4D$, and $4F$ populations have decayed into the $n=3$ manifold. Since electron-capture cross sections decrease with N and L, the cascade repopulation correction will be small and was neglected. The two higher frequency $n=3$ microwave transitions have no overlapping transitions in higher n states. The 1080-MHz $3\,^2D_{5/2}$-$3\,^2P_{3/2}$ transitions are affected by small overlapping resonances of 1240 and 1360 MHz ($4\,^2S_{1/2}$-$4\,^2P_{3/2}$ and $4P_{1/2}$-$4D_{5/2}$) which were subtracted. The Lamb-shift resonance $3\,^2S_{1/2}$-$3\,^2P_{1/2}$ was affected by unresolvable cascades and was not used in the data analysis. The possible stray electric (0.16 V/cm) and magnetic [20 mG($\vec{v}\times\vec{B}=0.06$ V/cm)] fields can cause mixing of the states and alter the field-free analysis used to derive Eq. (33). These fields will affect the most sensitive states (nearly degenerate $3\,^2P_{3/2}$ and $3\,^2D_{3/2}$ states) by less than 1% and thus were neglected. Since the target was operated in a regime where the signal depends linearly on the pressure, the affects of non-electron-capture collisions were negligible. Several other affects such as the first- and second-order Doppler shift were negligible.

C. Results

The data were fitted to Eq. (33) using an unconstrained least-squares-fitting program in which the cross sections are the only free parameters. The results from the fitting program for two configurations of the $N1$ data set are shown in Figs. 11 and 12 (all six configurations were fitted simultaneously). The agreement between the fitting function and the data was fairly good with χ^2/DF in the range from 2.8 to 4.8. From an analysis of each configuration separately, the major source of the discrepancy between the data and the fitting function was the inability to calculate correctly the line shapes in the perpendicular electric field configurations. Simulations of these line shapes showed that the linewidth was slightly dependent on the vertical beam location in the interaction region. The experimental uncertainty in the beam position was sufficient to explain the small differences between the data and the calculated fits. The simulations showed that when the whole line shape is analyzed, the extracted cross sections are not sensitive to small errors in the calculated line shapes. The data obtained from the short scans of the resonance peaks only were corrected by a small factor obtained from the full linescans so that the resultant analysis would not be affected by these small line-shape differences. The short scan data were taken with the same microwave power level as the full linescan data so there is no uncertainty in this correction due to power broadening. This uncertainty in the line-shape calculations could be reduced by utilizing a more collimated beam with improved alignment so that there is less uncertainty in the field sampled by the atoms traversing the interation region. The six extracted electron-capture cross sections $\sigma_{nL\,|M_L|}$ from the four data sets are tabulated in Table III. The three sets of cross sections obtained with the nitrogen target agreed with one another and were averaged. The cross sections for each gas were summed over $|M_L|$ and L to determine the cross sections for capture into a given L level, $\sigma_{3L}=\sum_{M_L}\sigma_{3L\,|M_L|}$, and into the whole $n=3$ manifold, $\sigma_3=\sum_L\sigma_{3L}$. The relative ratios were obtained from the fitting program and the absolute cross sections were calculated from the fit results, ϵ_{det}, ρL, and N/I. The errors in the relative cross sections were limited by χ^2/DF which was caused by the uncertainty in knowing the beam position in the interaction region. If the beam position is

TABLE III. A summary of the relative partial cross sections for the several sets of measurements with 49-keV protons incident on a nitrogen target and for the single set of measurements with a molecular hydrogen target. $\sigma(3,0)$ is the absolute cross section for capture into the S state in units of 10^{-18} cm^2.

Target / L,M_L	N_2-1	N_2-2	N_2-3	N_2 Average	H_2-1
0 0	1	1	1	1	1
1 0	0.48(9)	0.40(14)	0.46(9)	0.45(6)	0.20(12)
1 1	0.05(8)	0.08(9)	0.07(7)	0.07(7)	0.03(10)
all	0.58(14)	0.56(19)	0.60(13)	0.59(8)	0.26(18)
2 0	0.03(4)	0.01(6)	0.07(4)	0.04(2)	0.03(5)
2 1	0.03(3)	0.05(4)	0.01(3)	0.03(2)	0.02(4)
2 2	−0.02(1)	−0.01(2)	0.01(2)	−0.01(1)	0.00(2)
all	0.07(6)	0.09(9)	0.11(6)	0.08(4)	0.07(8)
χ^2/DF	2.8	3.9	3.0	3.8	4.8
$\sigma(3,0)$		6.5(3.4)			3.8(2.0)

TABLE IV. A comparison of the relative partial cross sections for charge capture into the $n=3,L$ states for 49-keV protons incident on molecular hydrogen and molecular nitrogen obtained in this experiment with those obtained in other experiments. $\sigma(3,0)$ is the absolute cross section for capture into the S state in units of 10^{-18} cm^2.

Target	State L M_L	This experiment	Hughes *et al.* (Ref. 19)	Ford *et al.* (Ref. 20)
H_2	0 0	1	1	1
	1 0	0.20(12)		
	1 1	0.03(12)		
	all	0.26(18)	0.13	1.13
	2 0	0.03(5)		
	2 1	0.02(4)		
	2 2	0.00(2)		
	all	0.07(8)	0.06	0.008
	$\sigma(3,0)$	3.8(2.0)	4.5(0.5)	5.5(1.4)
N_2	0 0	1	1	1
	1 0	0.45(6)		
	1 1	0.07(4)		
	all	0.59(8)	0.48(12)	0.57(18)
	2 0	0.04(2)		
	2 1	0.03(2)		
	2 2	−0.01(1)		
	all	0.08(4)	0.09(2)	0.09(3)
	$\sigma(3,0)$	6.5(3.4)	6.6(0.7)	7.0(1.8)

known better, the errors could be reduced by a factor of 2 and would be limited by statistics. An overall improvement of 5—10 in the quoted errors is probably achievable before other systematic errors become important. The uncertainties in the absolute cross sections could be improved with better determination of ϵ_{det} and ρ.

VI. CONCLUSIONS

The cross sections for electron capture into the $n=3$ manifold appear to be monotonically decreasing with increasing L and $|M_L|$ for both nitrogen and hydrogen. The total manifold cross section σ_3 is larger for nitrogen and this target produces relatively more $L\neq 0$ states than the hydrogen target. For both gases, the cross sections σ_3 are about 3% of the total electron-capture cross sections (for nitrogen $\sigma_T=3.5\times10^{-16}$ cm^2 and for hydrogen $\sigma_T=1.8\times10^{-16}$ cm^2).[29] This ratio is in agreement with the 3.1% ratio predicted from the simple n^{-3} scaling law for a capture into a manifold with principal quantum number equal to n.

Table IV shows a comparison of the σ_{nL} cross sections measured in this experiment with previously measured results obtained with the decay curve method.[19–21] The experiment of Ford *et al.* was for (75—400)-keV incident protons and was extrapolated to the 49-keV energy used in

TABLE V. A summary of the theoretical calculations of the partial cross sections for capture into the S, P, and D angular momentum states for the $n=3$ manifold of hydrogen for 50-keV protons incident upon an atomic hydrogen target. This table also gives the experimental values for capture from a molecular target divided by two on the assumption a hydrogen molecule is equivalent to two atoms of atomic hydrogen. CDW stands for continuum distorted wave, CIS for continuum intermediate state, and CAS for coupled atomic state.

Method	Reference	Cross section $\sigma(3,0)$ (10^{-18} cm^2)	$\frac{\sigma(3,1)}{\sigma(3,0)}$	$\frac{\sigma(3,2)}{\sigma(3,0)}$
Born *A*	31	2.4	1.50	0.21
Modified Born	32	2.2	1.27	0.38
Born *B*	33	2.6	1.00	0.12
CDW	34	4.6	0.43	0.10
CIS	35	5.6	1.30	0.18
CAS	36	4.5	0.30	0.05
Eikonal	37,38	2.5	1.52	0.24
Experiment/2		1.9(1.0)	0.26(18)	0.07(8)

TABLE VI. A comparison of the partial cross sections for charge capture into the $n=3$ state for 49-keV protons incident on a molecular hydrogen target with the CAS eikonal and OBK theoretical predictions (Refs. 36 and 38) for charge capture into the $n=3$ state for 49-keV protons incident on an atomic hydrogen target.

L	M_L	Experiment	CAS	Theory eikonal	OBK
0	0	1	1	1	1
1	0	0.20(12)	0.17	1.33	1.22
1	1	0.03(12)	0.064	0.113	0.120
	all	0.26(18)	0.30	1.556	1.46
2	0	0.03(5)	0.038	0.153	0.139
2	1	0.02(4)	0.0063	0.033	0.033
2	2	0.00(2)	0.0009	0.002	0.003
	all	0.07(8)	0.052	0.223	0.211

this experiment. All three experiments agree on the measured charge transfer cross sections for a nitrogen target; the experiment of Ford *et al.* disagrees with the present experiment and that of Hughes *et al.* on the $3P$ cross sections for a hydrogen target. Though the result of Hughes *et al.* is in agreement with the present experiment, caution must be exercised since our experiment was performed for only one energy. For the energy utilized in this experiment, there is some speculation that the results obtained with the molecular hydrogen target might be equivalent to a target of two separate atoms.[30] Table V shows a comparison of the present results (divided by two) with some of the calculations for electron capture by protons incident on an atomic hydrogen target.[31–38] This table shows that if the assumption of the equivalency between a hydrogen molecule and two hydrogen atoms is valid, then only the continuum distorted wave (CDW) and coupled atomic state (CAS) calculations agree satisfactorily with the experimental results for the relative cross sections for capture into the different angular momentum states.

Table VI shows a comparison between the partial cross section for capture into each of the angular momentum substates with the coupled atomic state calculations of Shakeshaft,[36] the eikonal calculation of Ho *et al.*,[38] and the Oppenheimer, Brinkman, Kramer's (OBK) calculation of Ho *et al.*[38] The agreement between the CAS calculation and the experimental results is quite satisfying in view of the large errors. The eikonal and OBK calculations disagree markedly with the experimental results. It is interesting that the partial cross sections for the eikonal and OBK calculations are almost the same and that the two calculations differ principally in the magnitude of the cross section for capture into the $n=3$ manifold. A rigorous comparison between experiment and various theories requires the measurement of the cross sections for an atomic hydrogen target. It would also be helpful to have measurements with greater precision.

This experiment has presented for the first time a complete determination of the $n=3$ electron-capture cross sections for 49-keV protons incident on molecular nitrogen and hydrogen. These cross sections give a complete description of the populations of the level in the $n=3$ manifold for excited atoms produced through charge capture. In future experiments, we plan to improve the accuracy with minor improvements in the apparatus. We then plan to study excited-state electron capture as a function of energy for capture into other manifolds and for different target gases including atomic hydrogen. This should provide a rigorous test of our understanding of electron capture involving protons incident on hydrogen atoms.

ACKNOWLEDGMENTS

This research was supported in part by the National Science Foundation under Grants Nos. PHY-78-09657 and PHY-80-26547.

*Present address: Plasma Physics Laboratory, Princeton, NJ 08544.

[1]F. M. Pipkin, in *Atomic Physics 4,* edited by G. zu Putlitz, E. W. Weber, and A. Winnacker (Plenum, New York, 1975), p. 119.

[2]F. M. Pipkin, in *Beam Foil Spectroscopy,* edited by I. A. Sellin and D. J. Pegg (Plenum, New York, 1976), Vol. I, p. 271.

[3]E. N. Fortson and L. Wilets, in *Advances in Atomic and Molecular Physics,* edited by D. R. Bates and B. Bederson (Academic, New York, 1980), Vol. 16, p. 367.

[4]H. B. Gilbody, in *Advances in Atomic and Molecular Physics,* edited by D. R. Bates and B. Bederson (Academic, New York, 1979), Vol. 15, p. 293.

[5]A. Dalgarno, in *Advances in Atomic and Molecular Physics,* edited by D. R. Bates and B. Bederson (Academic, New York, 1979), Vol. 15, p. 37.

[6]B. H. Bransden, in *Advances in Atomic and Molecular Physics,* edited by D. R. Bates and B. Bederson (Academic, New York, 1975), Vol. 15, p. 263.

[7]D. Basu, S. C. Murherjee, and D. P. Sural, Phys. Rep. 42, 145 (1978).

[8]Dz. Belkic, R. Gayet, and A. Salin, Phys. Rep. 56, 279 (1979).

[9]J. Delos, Rev. Mod. Phys. 53, 287 (1981).
[10]K. Tokayanagi and H. Suzuki, *Cross Sections for Atomic Process* (Research Information Center, Nagoya University, Nagoya, Japan, 1976, 1978), Vols. I and II.
[11]F. J. De Meer, in *Atomic and Molecular Processes in Controlled Thermonuclear Fusion,* edited by M. R. C. McDowell and A. M. Ferendeci (Plenum, New York, 1980), p. 351.
[12]A. Salin, Comments At. Mol. Phys. 9, 165 (1980).
[13]C. D. Lin, Comments At. Mol. Phys. 11, 261 (1982).
[14]W. Fritsch and C. D. Lin, J. Phys. B 15, 1255 (1982).
[15]V. Maruhn-Rezwani, N. Grün, and W. Scheid, Phys. Rev. Lett. 43, 512 (1979).
[16]A. Dalgarno (private communication).
[17]T. J. Morgan, J. Geddes, and H. B. Gilbody, J. Phys. B 6, 2118 (1973).
[18]J. E. Bayfield, in *Atomic Physics 4,* edited by G. zu Putlitz, E. W. Weber, and A. Winnacker (Plenum, New York, 1975), p. 397.
[19]R. H. Hughes, C. A. Stigers, B. M. Doughty, and E. D. Stokes, Phys. Rev. A 1, 1424 (1970).
[20]J. C. Ford and E. W. Thomas, Phys. Rev. A 5, 1694 (1972).
[21]J. C. Ford and E. W. Thomas, Phys. Rev. A 5, 1701 (1972).
[22]H. Ooona and W. S. Bickel, Nucl. Instrum. Methods 90, 223 (1970).
[23]R. J. Knize, S. R. Lundeen, and F. M. Pipkin, Phys. Rev. Lett. 49, 315 (1982).
[24]M. P. Silverman and F. M. Pipkin, J. Phys. B 7, 704 (1974).
[25]M. P. Silverman and F. M. Pipkin, J. Phys. B 7, 730 (1974).
[26]M. P. Silverman and F. M. Pipkin, J. Phys. B 7, 747 (1974).
[27]R. Knize, Ph.D. thesis, Harvard University, 1981 (unpublished).
[28]W. Heitler, *The Quantum Theory of Radiation* (Oxford University Press, London, 1954).
[29]S. K. Allison, Rev. Mod. Phys. 30, 1137 (1958).
[30]F. Gerjuoy, Rev. Mod. Phys. 33, 544 (1961).
[31]D. R. Bates and A. Dalgarno, Proc. Phys. Soc. London, Sect. A 66, 972 (1953).
[32]Y. Band, Phys. Rev. A 8, 2857 (1973).
[33]T. G. Winter and C. C. Lin, Phys. Rev. A 10, 2141 (1974).
[34]Dz. Belkic and R. Gayet, J. Phys. B 10, 1911 (1977).
[35]Dz. Beklic, J. Phys. B 10, 3491 (1977).
[36]R. Shakeshaft, Phys. Rev. A 18, 1930 (1978).
[37]F. T. Chan and J. Eichler, Phys. Rev. A 20, 1841 (1979).
[38]T. S. Ho, D. Umberger, R. L. Day, M. Lieber, and F. T. Chan, Phys. Rev. A 24, 705 (1981).